High Energy Density Physics 7 (2011) 130–140

Contents lists available at ScienceDirect

High Energy Density Physics

journal homepage: www.elsevier.com/locate/hedp

Review

Radiative effects in radiative shocks in shock tubes

R.P. Drake [a,*], F.W. Doss [a], R.G. McClarren [b], M.L. Adams [b], N. Amato [b], D. Bingham [c], C.C. Chou [a], C. DiStefano [a], K. Fidkowski [a], B. Fryxell [a], T.I. Gombosi [a], M.J. Grosskopf [a], J.P. Holloway [a], B. van der Holst [a], C.M. Huntington [a], S. Karni [a], C.M. Krauland [a], C.C. Kuranz [a], E. Larsen [a], B. van Leer [a], B. Mallick [b], D. Marion [a], W. Martin [a], J.E. Morel [b], E.S. Myra [a], V. Nair [a], K.G. Powell [a], L. Rauchwerger [b], P. Roe [a], E. Rutter [a], I.V. Sokolov [a], Q. Stout [a], B.R. Torralva [a], G. Toth [a], K. Thornton [a], A.J. Visco [a]

[a] University of Michigan, Ann Arbor, MI 48109, USA
[b] Texas A&M University, College Station, TX, USA
[c] Simon Fraser University, Vancouver, British Columbia, Canada

ARTICLE INFO

Article history:
Received 7 March 2011
Accepted 7 March 2011
Available online 21 March 2011

Keywords:
Radiative shocks
Laboratory astrophysics
Radiation transfer
Shock waves

ABSTRACT

Using modern high-energy-density facilities it is straightforward to produce radiative shock waves in which the transfer of energy by radiation controls the hydrodynamic structure of the system. Some of these experiments use shock tubes. This paper discusses such experiments, with an emphasis on the simple physical relations that determine the primary features of such shocks and on the details and impact of radiative energy transfer in such systems. Notable aspects include the creation of high-density shocked layers, the flow of radiative energy toward regions of higher energy density, and the creation of secondary shocks by ablation of the tube walls ahead of the primary shock front. Simulations of one such experimental system are also shown.

1. Introduction

Radiative shocks abound in the universe, being present whenever shocked matter becomes hot enough that radiative energy transfer changes the structure of the shock. The shock wave that causes a star to explode following core-collapse is radiative, both as it propagates through and as it emerges from the star [1,2]. The ejecta from supernovae can itself develop into a radiative shock [4,5] and also can drive radiative shocks into dense matter [3,4]. Aging supernova remnants eventually enter a radiative phase [6]. Clumps of material propagating up astrophysical jets also may drive radiative shocks [7]. All these shock waves are said to propagate into unshocked, "upstream" matter and to produce shocked, "downstream" matter. The radiation heats the material ahead of the increase in density produced by the shock wave, creating a region described as a "radiative precursor".

With the advent of experimental facilities that produce high-energy-density conditions, laboratory studies of radiative shocks have become an active area of research. Many of these experiments [8–30] have used an energy source to launch a non-radiative plasma piston that drives a radiative shock wave in a gas or a foam whose density is $\ll 1\ \mathrm{g/cm^3}$. Such shock waves can be produced in shock tubes, where the intent is to limit the lateral expansion of the shocked material and thus to sustain the shock strength. Our focus here will be on shock waves in shock tubes under conditions that allow observation of the shocked matter. Some other laboratory radiative shocks are produced when a plasma expanding from a surface drives a radiative shock [31–34]. In yet other cases, local deposition of energy produces shock waves that exhibit radiative effects [35–38].

Theoretical studies of radiative shocks date to the 1950s [39,40], and have developed further in parallel with increasing computational capability. Various regimes of radiative shocks have been identified [16,41], depending on how readily the radiation escapes the shocked material and on the ratio of radiation pressure to material pressure. Most theoretical research [42–52] has addressed the evolution of steady shock waves under "optically thick" conditions, in which the extent of the system is many mean free paths for the thermal radiation so that the radiation is deeply trapped in the material. Some theoretical research has addressed the behavior of shock waves under "optically thin" conditions, in which the radiation readily escapes from the shocked matter

* Corresponding author.
E-mail address: rpdrake@umich.edu (R.P. Drake).

1574-1818/$ – see front matter © 2011 Elsevier B.V. All rights reserved.
doi:10.1016/j.hedp.2011.03.005

[53–56]. Recent theoretical work [57] has also addressed the experimentally more relevant case in which the shocked matter is optically thick while the unshocked matter is optically thin.

In the following, Section 2 discusses the fundamental, "back of the envelope" description of this type of radiative shock in a specific configuration that we have studied extensively. Section 3 then discusses the axial structure of these shocks showing that their final compressed density is determined fundamentally by energy balance. Next, Section 4 discusses the radiation transfer within these shocks. The hot, optically thin layer they produce creates unusual features in both the density structure and the transfer of radiation. Following this, Section 5 discusses the effects of the radiation from the hot, shocked matter on the shock-tube walls ahead of the shock front. This interaction produces a complex flow whose features may be used to diagnose some of the properties of the system. Section 6 summarizes our work to simulate the behavior of such shocks and shows results of such simulations. We will not discuss here our related work to evaluate the predictive capability of the simulation code in the context of these radiative shocks [58,59]. Following this, Section 7 concludes the paper.

2. Fundamental elements of driven radiative shocks

Fig. 1 shows photographs of two laser targets used in our laboratory studies of radiative shocks. These targets are assembled at the University of Michigan, where precision machining techniques are used to assure correct target orientation [60]. This has proven essential to obtain shocked layers that are not significantly tilted with respect to the shock tube. The two targets shown in the figure have the same inner details and produce nearly identical radiative shocks; the differences in target structure relate to the diagnostics used for specific experiments. Here we discuss the inner details and resulting properties of one specific case of such a target. Fig. 2 shows the essential details of our standard targets. We have used similar targets for an extensive sequence of experimental campaigns [12,16,19,22,23,26,28–30].

Ten laser beams from the Omega laser facility [62] irradiate a 20 μm thick Be disk with 0.35 μm-wavelength light, whose "critical density" of free electrons, below which the light is

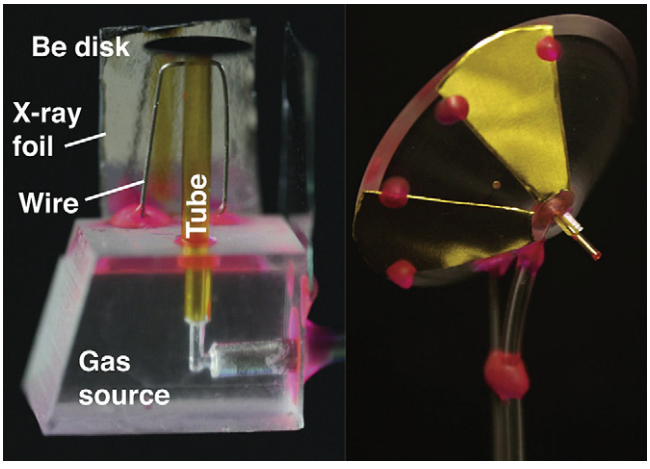

Fig. 1. Laser targets used to produce radiative shocks. In the target on the left, one can see the Be disk. Here the lasers would enter from above. Some components are labeled. Other lasers strike the x-ray foil to produce x-rays for a diagnostic; the wire provides it with a spatial fiducial. To irradiate the target on the right, the laser beams enter the conical acrylic shield, from the upper left. The shock tube in the target on the right is the small object extending toward the lower right. Fiducial grids are attached to it. The wedges of gold attached to the acrylic cone protect the ungated imaging diagnostic [61] from emissions from the laser-produced plasma.

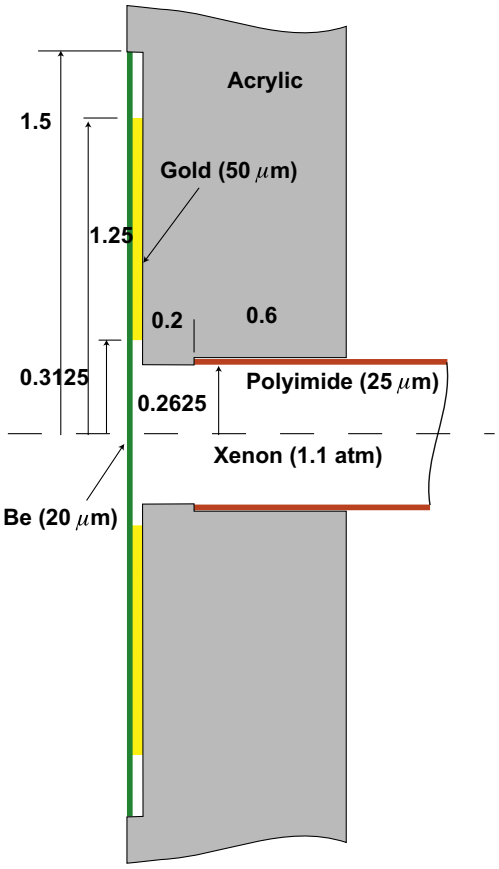

Fig. 2. Details of the interior portion of a standard radiative shock target. The layer of gold exists to retard the progress of the laser-driven shock at radii outside the shock tube. Nominal dimensions are given in mm.

absorbed, is 8.9×10^{21} cm^{-3}. The duration of the (flat-topped) laser pulse is 1 ns, with 4 kJ of energy on an ~800 μm diameter spot, so that the irradiance is $\sim 7 \times 10^{14}$ W/cm^2 = $\sim 7 \times 10^{21}$ ergs/s/cm^2. Most of the energy is absorbed, so the absorbed energy fluence in 1 ns is $\sim 7 \times 10^{12}$ ergs/cm^2. Some of the absorbed laser energy is transported by electron heat conduction to high density, where it ablates the dense material. The corresponding pressure of ~50 Mbars, which is $\sim 5 \times 10^{13}$ dynes cm^{-2}, first drives a shock wave through the Be disk for ~500 ps and then accelerates the shocked material for the remainder of the laser pulse.

The purpose of shocking and then accelerating the Be is to produce a high-velocity piston that will drive a shock wave down the Xe tube. The "hydrodynamic efficiency" of the conversion from laser energy to kinetic energy is around 10%, giving a kinetic energy fluence of 7×10^{11} ergs/cm^2. In round numbers, the energy is absorbed below critical density, half of it goes up to solid density where the ablation occurs, removing about 20% of the target mass, corresponding to a 20% rocket efficiency for the energy reaching that density. The implied kinetic energy fluence of $\sim 7 \times 10^{11}$ ergs/cm^2 is carried by what was initially about 16 μm of Be at 1.8 g/cm^{-3}, giving an areal mass density of $\sim 3 \times 10^{-3}$ g/cm^2 a thus an initial velocity of $v \sim 2 \times 10^7$ cm/s (200 km/s). Simulations and long-term observations suggest that the average velocity of the Be plasma is never quite this high, but that the leading edge of the expanding Be plasma can cause the shock to reach ~200 km/s for a brief period of time. The average shock velocity over 26 ns is observed to remain above 100 km/s.

The "piston" of Be plasma drives a strong-shock wave through the Xe. One can infer from basic strong-shock relations [63] some of the properties of the shocked Xe. The initial xenon gas density is

$\rho = 0.0065$ g/cc, so the post-shock Xe pressure is $\sim\rho v^2 \sim 2\times10^{12}$ dynes/cm$^2 = 2$ Mbars. The initial shock heating goes into the ions, so the initial ion temperature is $k_B T_{ii} \sim 0.1 A m_p v^2$, with atomic mass $A = 131$ and proton mass m_p, with Boltzmann constant $k_B = 1.6\times10^{-12}$ ergs/eV, so $T_{ii} \sim 2$ keV. The factor of 0.1 is approximate and depends in detail upon the ionization and effective polytropic index. Fig. 3 shows an example of the shock structure observed at 26 ns; it can provide a geometric reference for the following discussion.

The dynamics near the shock front and the ionization are complex. The density jump at the shock front occurs on a spatial scale of less than 10 ion–ion mean free paths. This corresponds to a ~0.1 femtosecond timescale. The energy exchange between electrons and ions is a few times slower than this, and the energy from each ion is shared with Z electrons, where Z is the average ionization. One can estimate the resulting electron temperature, T_{es}, and Z using the Saha equation [63], assuming that radiative losses are unimportant on this timescale. This is an oversimplification: radiative losses matter but are not dominant [23]. One can write the resulting equation for Z as

$$Z = \sqrt{\frac{k_B T_e}{E_H}}\sqrt{\ln\left[\frac{1}{n_e}\frac{1}{4a_o^3}\left(\frac{k_B T_e}{\pi E_H}\right)^{3/2}\right]} - \frac{1}{2}, \quad (1)$$

in which n_e is the electron density, $a_o = 5.29\times10^{-9}$ cm is the Bohr radius, E_H is the ionization potential of hydrogen, and one has assumed equal statistical weights of adjacent ionization states. For the present problem, one has $T_e = T_{es} = T_{ii}/(Z+1)$ and $n_e = n_i Z$, where the ion density is n_i, from which one has

$$Z = 19.7\sqrt{\frac{T_{ii}}{(Z+1)}\left[1 + 0.19\ln\left(\frac{10^{24}T_{ii}^{3/2}}{(Z+1)^{3/2}Zn_i}\right)\right]} - \frac{1}{2}, \quad (2)$$

with T_{ii} in keV and n_i in units of cm^{-3}. Such a model, with $T_{ii} = 2$ keV and $n_i = 2\times10^{20}$ cm^{-3}, gives $Z = 10.3$ and $T_{es} = 180$ eV.

However, energy balance implies that this cannot be the final state. The energy flux available to create the radiative and material energy fluxes produced by the shock is the incoming kinetic energy flux seen from the shock frame (a frame of reference in which the shock is stationary). This energy source is $\sim\rho v^3/2$, which is

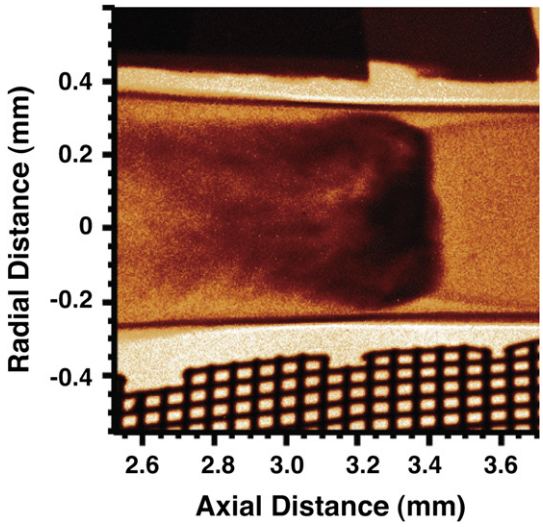

Fig. 3. Radiographic image of one of our base radiative shocks at 26 ns. The shock is moving from left to right within the shock tube, whose walls are expanding behind the shock. Above and below the shock tube, respectively, are structures for intensity calibration and spatial calibration. The radiograph was obtained using He$_\alpha$ emission from a backlit-pinhole V source [28].

$\sim3\times10^{19}$ ergs/cm^2/s for the present case. If the final state of the shocked material, which rapidly becomes optically thick, were to emit radiation at a 180 eV temperature, then $\sigma T_{es}^4 \sim 10^{21}$ ergs/cm^2/s, about 30 times larger than the incoming kinetic energy flux. Here the Stefan Boltzmann constant σ is $\sim10^5$ W/cm^2/eV$^4 = 10^{12}$ ergs/cm^2/s/eV^4. The implication is that the actual radiation emission must be much less than σT_{es}^4 for this initial value of T_{es} Instead, there must be an optically thin cooling layer (of optical depth τ) through which the temperature declines to a final value T_f. The emission from this cooling layer is then $\sim\tau\sigma T_{es}^4$ in the upstream direction.

In the absence of any radiation that escapes from the shocked material downstream of the cooling layer and of any final downstream flux of material energy, one would have $2\tau\sigma T_{es}^4 = \rho v^3/2$, where the factor of 2 is because the cooling layer emits equally in both directions. This would give $\tau\sim(1/2)\times(1/30)$ based on the previous paragraph. In fact τ is smaller than this because there is radiation that escapes from by the downstream shocked matter, and there is some final downstream flux of material energy. In the limit that the shocked material can be taken to be semi-infinite, there must be no net radiation flux within the downstream material, so the downstream radiation flux from the cooling layer must equal the upstream flux from the final state. This implies $\tau\sigma T_{es}^4 = \sigma T_f^4$. Because the cooling layer radiates equally in both directions, and the radiation from the final state flows nearly unimpeded through it, the radiation leaving the shocked matter in the upstream direction is approximately $\tau\sigma T_{es}^4 + \sigma T_f^4 = 2\sigma T_f^4$. Assuming that the downstream material energy flux is negligible one can estimate the final temperature by setting $2\sigma T_f^4 = \rho v^3/2 \sim 3\times10^{19}$ ergs/cm^2/s. This implies with the above $T_f \sim 60$ eV. The case of a semi-infinite downstream region is treated in detail by McClarren et al. [57], who confirm the results of the simple analysis just given.

For the specific case here, based on the Rosseland mean opacity, the mean free path of the radiation in the shocked Xe is several μm and the final Xe density is ~25 times the initial density, so that as the shock wave travels a few mm the optical depth of the shocked Xe layer reaches tens. Radiation hydrodynamic simulations in 1D suggest that about 50% of the incident energy flux is radiated back upstream, about 20% of it is radiated downstream from the downstream boundary of the shocked layer, and about 30% of it is carried downstream as material energy.

Returning to simple arguments, in the face of the cooling caused by the radiative energy losses, the density of the shocked Xe must increase to balance the ram pressure of the incoming flow as seen in the shock frame. For an initial and final mass density ρ_o and ρ_f, respectively, this implies $\rho_f R T_f \sim \rho_o v^2$, so that the compression is $\rho_f/\rho_o = v^2/(RT_f)$, where R is the gas constant, given approximately by $R = (Z+1)k_B/(Am_p)$. Substituting values from the numbers given above, one finds a compression of 80. Using a velocity corresponding to times of observation, one obtains a compression near 40, which is also consistent with values from 1D simulations. The compression seen by line-integrated measurements near 13 ns [29] is nearer to 20; it is unclear at present whether this is because the shocked layer has been wrinkled by instabilities or because some other effect limits the compression.

The radiation striking the wall of the shock tube just ahead of the primary shock corresponds to roughly the irradiance of a 60 eV blackbody (being $\sim2\sigma T_f^4$ over about π sr). This is $\sim10^{12}$ W/cm^2 ($\sim10^{19}$ ergs/s/cm^2), which is sufficient to ionize the wall material and produce a plasma expansion from the wall. This plasma expansion in turn drives a "wall shock" into the Xe, as is discussed further below in Section 5. These wall shocks in turn interact with the primary shock, and the Xe that first enters a wall shock ends up moving more slowly than the primary shock, so that it produces a shell of entrained Xe that trails the primary shock.

One can see several of the above elements in the radiographic image of Fig. 3. The dark region within the shock tube shows where the shocked Xe is. The primary shock is the vertical boundary, which has traveled 3.4 mm in 26 ns, corresponding to an average velocity of 130 km/s. The shell of entrained, shocked Xe is evident; it produces the limb-darkened features near the shock tube wall and to the left of the primary shock. Near the shock-tube axis, the darkest zone corresponds to the accumulated Xe that has been shocked only by the primary shock. This region is clearly less than 200 μm thick, and thus corresponds to a compression above 17. In addition, the region of accumulated Xe appears to be clustered near the tube axis; we comment further on this in Section 6 below. To the right of the primary shock, the wall shock is clearly visible as a dark, curved feature extending from the wall to the kink in the primary shock. The comparatively bright triangle of material between this kink and the shock tube is expanded plastic material from the wall; the plastic is more transparent to the diagnostic x-rays than is the Xe gas.

The final observations we will make in this section concern the precursor region in the Xe. First consider heating of this region. Photons at 60 eV have an energy of $\sim 10^{-10}$ ergs, so the upstream photon flux is $\sim 3 \times 10^{29}$ photons/cm^2/s. The incoming ion flux is $\rho v/(Am_p) \sim 10^{27}$ ions /cm^2/s. The implication is that there are more than enough photons to ionize and heat the gas before the shock reaches it. This does not however guarantee that such ionization will happen. In actual experiments in shock tubes, the photon flux decays as photons escape laterally, with a spatial scale of order the shock-tube radius r_{st}. In the specific experiment we have been discussing, r_{st} is ~300 μm. Since only a fraction of a percent of the photon flux is required to ionize all the incoming atoms, the requirement is that the photon mean free path must not be much more than about 100 times r_{st}. In the present case the mean free path is about a third of r_{st}, so the precursor will be ionized.

Second consider the energy flux carried back through the density jump in consequence of heating of the precursor region. If this energy flux were large, then the simple arguments given above which ignored it would become less accurate. For $Z \sim 10$ at a temperature of 60 eV, the thermal energy flux carried to the shock front by the inflowing matter is $\sim 10^{27}$ ions /cm^2/s $\times$ 11 particles per ion $\times 10^{-10}$ ergs $\sim 10^{18}$ ergs/cm^2/s. This is a few percent of the incident kinetic energy flux and upstream radiation flux. This is why the thermal energy in the precursor can be ignored to a first approximation. The story regarding radiation emission from the precursor is more complex. In experiments [15,25] using Xe gas at densities below 1 mg/cm^3, the radiation mean free path in the precursor is large compared to the scale of the heated precursor region so emission from the precursor is definitely negligible. In our experiments discussed here, the 2D simulations below find that the scale of the decrease of σT_e^4 in the precursor is ~100 μm. This is determined by radial energy losses; 1D simulations show much flatter precursor profiles. The radiation mean free path in the precursor is of the same order, also being ~100 μm. Thus, although the radiation does escape readily in the region upstream of the shock front, there is likely to be some "recycling" of the radiative energy back through the shock front. However, this will remain small enough to be a secondary effect.

The approximate energies involved here are summarized in Table 1. The kinetic energy flowing into the shock is over ~10 ns at an average energy flux of ~half the early-time value estimate above.

Table 1
Energies in radiative shocks on Omega.

Laser Energy	4000 J
Be Kinetic energy	400 J
Shock frame kinetic energy	40 J
Forward radiated energy	20 J

3. Shock structure

We turn now to a more detailed discussion of the axial structure in the shocked layer. There is an interplay of energy flow by radiative transfer and hydrodynamic evolution of the fluid. Treating the system as one-dimensional, the shock as a steady shock, and the material as a polytropic gas with index γ, the conservation of mass, momentum, and energy in the shock frame imply

$$\rho u = -\rho_o u_s, \tag{3}$$

$$\rho u^2 + p = -\left(\rho_o u_s\right) u + p = \rho_o u_s^2 + p_o, \quad \text{and} \tag{4}$$

$$F_R + \frac{\gamma}{\gamma - 1} p u + \frac{\rho u^3}{2} = -\frac{\rho_o u_s^3}{2} - \frac{\gamma}{\gamma - 1} p_o u_s + F_{Ro}, \tag{5}$$

respectively, in which the shock velocity is $u_s > 0$ but the upstream flow proceeds in the negative direction, mass density is ρ, the flow velocity is u, the pressure is p, and the (rightward) radiation energy flux is F_R. We designate any arbitrary point in the flow with no index, using indices o for the initial state, f for the final state, i for the state immediately downstream of the density jump, and otherwise as appropriate. In the third of these equations, the right-hand side represents the energy flux incident on the shock from upstream, and based on the arguments from Section 2 we know that p_o is small by comparison to the post-shock pressure. However, p_o does turn out to affect the final state as is described below. In addition, here we make the idealized assumption that the electron-ion equilibration happens rapidly by comparison to any radiative cooling, so that the material has only one temperature, T.

We define the normalized pressure as $p_n = p/(\rho_o u_s^2)$, the normalized specific pressure (proportional to specific thermal energy) as $RT_n = RT/u_s^2$, where R is the gas constant (here assumed to be constant for simplicity) so $p = \rho RT$, and the normalized radiation flux as $F_{Rn} = 2F_R/(\rho_o u_s^3)$. Defining the inverse compression, $\eta = \rho_o/\rho$, Eqs. 3–5 imply that

$$p_n = (1 - \eta) + p_{on}, \tag{6}$$

$$RT_n = \eta(1 - \eta) + p_{on}\eta, \quad \text{and} \tag{7}$$

$$F_{Rn} - F_{Ron} = -1 + \frac{2\gamma}{\gamma - 1}(\eta - p_{on}(1 - \eta)) - \frac{\gamma + 1}{\gamma - 1}\eta^2. \tag{8}$$

These equations illustrate a remarkable feature of radiative shocks: the structure of all the parameters is tightly coupled so that any one of η, p_n, RT_n and $(F_{Rn} - F_{Ron})$ implies all the others. No matter what the details of the radiation transport may be, they cannot independently set the temperature and the density in the system.

The structure of the right-hand side of the energy equation in this group is of interest, and is shown in Fig. 4 for $p_{on} = 0$. The density jump at the shock front moves the system to the left of the maximum of this curve. In the idealized case of a semi-infinite downstream region, the local radiation flux F_{Rn} approaches zero and the maximum density of the shocked material corresponds to the value of η for $(F_{Rn} - F_{Ron}) = -F_{Ron}$. In this case the density changes rapidly in the cooling layer (which must be optically thin as discussed in Section 2) and then soon reaches a final, constant value in the downstream final state. This idealized case is discussed in detail in [57].

One can also connect the argument of Section 2 regarding energy balance to these equations. There is some definite

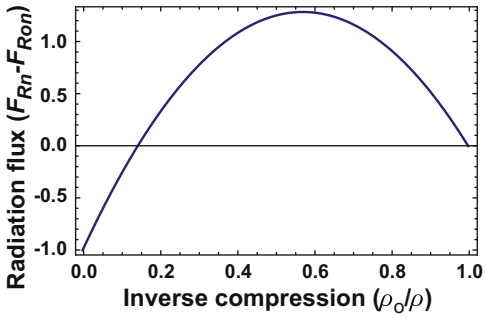

Fig. 4. The net rightward radiation flux is a deterministic function of the inverse compression, $\eta = \rho_o/\rho$. Shown for $\gamma = 4/3$.

connection between the radiative fluxes in the system and the temperature. The exact form of this connection may vary. For an optically thick, constant-density downstream region the upstream radiation flux from this final state must be $F_{Rf} = \sigma T_f^4$, connecting Eqs. 7 and 8. The arguments of Section 2 then still apply, so that the escaping rightward energy flux is $F_{Ro} = 2\sigma T_f^4$. In addition, for strong radiative shocks the upstream medium tends to heat until $T_o \sim T_f$ so $RT_f \sim p_{on}$ and from Eq. 7 one finds $\eta_f \sim RT_f$. With this connection, Eqs. 7 and 8 can then be solved to find

$$\eta_f = \frac{1}{2}\sqrt{\frac{\sqrt{8Q+1}-1}{Q}}, \tag{9}$$

where the normalized shock strength is $Q = 2\sigma u_s^5/(\rho_o R^4)$, which for typical experiments is quite large ($\sim 10^5$), and $\eta_f \sim (2Q)^{-1/4}$. For $Q \sim 10^5$ one finds $\rho_f \sim 20\rho_o$, which is in the ballpark of other estimates.

In the more typical case for experiments, the downstream region is not semi-infinite and the shock is only quasi-steady and is slowly decelerating. The density still increases rapidly through the cooling layer, but there are two competing effects in the downstream region. First, some radiation escapes the left boundary. This causes F_{Rn} to pass through zero and reach some final negative value F_{RLn}. The effect of this is to cause the density to increase slowly through the optically thick downstream region as the system follows the curve in Fig. 4. Second, the deceleration causes the ram pressure to decrease with time so that material that has been shocked expands and decreases in density. Depending on the competition between deceleration and leftward energy loss, it would not be surprising to see either a positive or a negative gradient in the density of the shocked layer of a given experimental system.

Another element of actual experiments is that the shocked material is not initially optically thick. So long as such material is optically thin it will continue to cool and to increase in density. However, once the material becomes optically thick, which will happen after the shock has propagated ~ 100 μm in the Omega experiments or ~ 1 mm in experiments such as those of [15] using lower gas pressures, the final density and temperature will be determined by the energy balance considerations discussed above. In consequence, the initial layer of shocked material may reach a final state that is denser than that of the material that is shocked later. One sees this effect at times in simulations, but no experiment yet has had the resolution to look for it.

The result of the dynamics just discussed is that these systems produce a relatively thin layer of dense material that is decelerating. One might anticipate that such a layer would be subject to the sort of instabilities described by Vishniac [64] and by Ott [65]. However, the shocked layer in present-day experimental systems is not so thin that the assumptions of these theories apply. To find a modified theory that is relevant to shocked, decelerating layers of finite thickness one must instead consider how the transverse waves on the shock front couple to the gravity waves on the rear surface of the shocked layer. This has been undertaken by Doss et al. [66], who find growing modes under experimental conditions. These may explain the structure observed in the experimental shock waves.

4. Radiation transport

It is remarkable that so much of the behavior of these shocks, as elucidated in Section 3, does not depend upon the details of the radiation transport. However, the detailed structure of the shocked material does depend upon the radiation transport, and the radiation transport turns out to have some challenging and interesting aspects. We discuss these here.

The problem for a complete theory of these shocks is to find equations that enable a precise determination of F_R in the fluid equations. One evidently cannot use an equilibrium diffusion model, as the cooling layer is a zone in which the transport is not diffusive and the radiation and matter are not in equilibrium. To understand the issues with other models, it is helpful to start with the radiative transfer equation written here as

$$\frac{1}{c}\frac{\partial I_R}{\partial t} + \frac{\partial I_R}{\partial s} = \int \kappa_\eta (B_\nu - I_\nu)\mathrm{d}\nu + \int \sigma_\nu (J_\nu - I_\nu)\mathrm{d}\nu, \tag{10}$$

in which the radiation intensity (energy flux per sr) is I_R, the path of the radiation is described by s, c is the speed of light, and the integrals are over all frequencies ν. Within the integrals, the subscript ν indicates spectral dependence with units as appropriate. The functions involved are the absorption opacity κ_ν, the scattering opacity σ_ν, the spectral thermal intensity (the Planck function) B_ν, the spectral radiation intensity I_ν, and the mean of the spectral intensity over all solid angle, J_ν. This equation is written in the geometric-optics limit, which is relevant to radiative shocks, and under the assumption that the scattering is elastic and isotropic. It can be viewed fundamentally as a kinetic equation for the photons. We will ignore the time-dependent term because the radiation reaches steady state instantaneously on the timescales of material motion.

Assuming only isotropic, elastic scattering and steady state, the zeroth moment over angle of the radiative transfer equation gives

$$\partial F_R/\partial z = 4\pi\kappa_P (B - J_R) \tag{11}$$

in one dimension, in which the thermal intensity is B, J_R is the mean radiation intensity averaged over all solid angle, $J_R = \int_{4\pi} I_R d\Omega/(4\pi)$, with radiation intensity (energy flux per sr) I_R, and Planck mean opacity κ_P, with units of inverse length and assumed as usual to be accurate for J_R in addition to B. For isotropic radiation, this equation describes the radiation-matter energy exchange in textbook non-equilibrium-diffusion models. To close the full set of equations, however, one still needs an additional constraint on J_R. A very common approach is to use a (single-group or multigroup) diffusion model based on the steady state, non-relativistic first moment in photon direction of the radiation transfer equation for isotropic emission,

$$\frac{\partial p_R}{\partial z} = -\frac{\overline{\chi}}{c}F_R, \tag{12}$$

in which $\overline{\chi}$ is an averaged opacity typically approximated as the Rosseland mean opacity, c is the speed of light, and p_R is the scalar radiation pressure. A common way to avoid introducing yet another variable and requiring yet another equation for closure is to work in the Eddington diffusion approximation, writing $p_R = f_E E_R = f_E(4/c)J_R$, in which E_R is the radiation energy density. Eq. 12 then becomes

$$4\pi f_E \frac{\partial J_R}{\partial z} = -\overline{\chi} F_R, \tag{13}$$

where the Eddington factor f_E is assumed to be constant and is 1/3 for an isotropic radiation intensity distribution and 1 for a beamlike one. Eq. 13, combined with Eq. 11, closes the system of equations. This provides a sensible approach to finding the structure of any region that is many optical depths in extent, which assures that the radiation intensity distribution is nearly isotropic.

However, within the cooling layer of radiative shocks, the angular distribution of the radiation is distinctly non-isotropic. We give an example of this for a model system in Fig. 5. The parameters of this system are that there is a semi-infinite layer to the left of temperature 1 unit, a hot, thin layer of optical depth 0.1 with temperature 4 units, and a semi-infinite layer to the right of temperature 0.5 units. The figure shows the angular distribution of the radiation at the center of the hot layer for three values of the lateral optical depth. We include the lateral optical depth because this quantity is finite in any experiment using a shock tube. (However, even in curved shocks produced at low gas pressure, the effective lateral optical depth will tend to be larger than 1.) One sees that the radiation is significantly anisotropic under all the cases shown. More realistic cases relative to the experiment, having hot layers that are thinner, retain very anisotropic intensity distributions but have a smaller angular zone near the vertical axis where there is significant anisotropy.

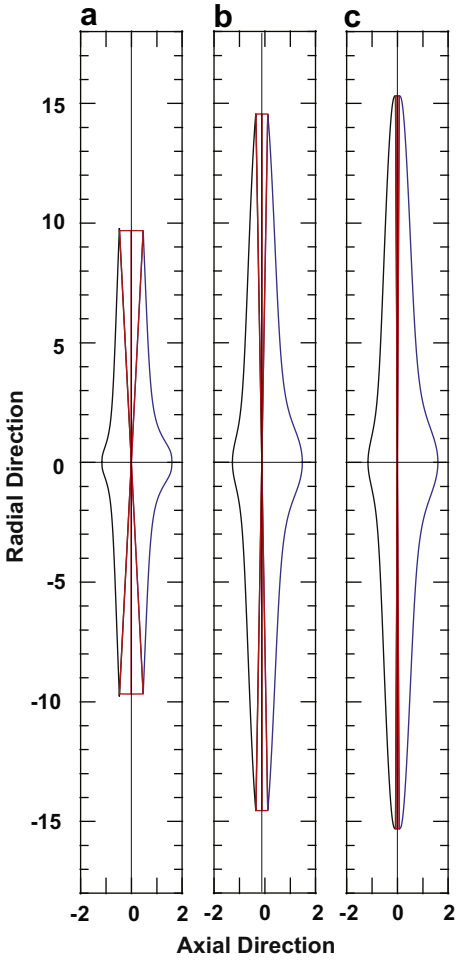

Fig. 5. Polar plots showing the angular distribution of radiation intensity at the center of a hot, optically thin layer between two cooler layers. The lateral optical depth of the system is (a) 1, (b) 3, and (c) 10. The red portions of these curves, near the vertical axis, show the range of angles over which the emission is entirely from the shocked layer. (For interpretation of the references to colour in this figure legend, the reader is referred to the web version of this article.)

When one evaluates the moments of the radiation distribution for systems having this structure, one finds that J_R is very nearly constant throughout the thin layer but is in fact peaked at the center. In contrast,

$$p_R = 2\pi \int_{-1}^{1} \mu^2 I_R \mathrm{d}\mu/c \quad \text{and} \tag{14}$$

$$F_R = 2\pi \int_{-1}^{1} \mu I_R \mathrm{d}\mu, \tag{15}$$

change monotonically through the layer, with p_R declining from the hotter edge toward the cooling edge. Note that both p_R and F_R underweight the contributions near $\mu = 0$ by comparison to J_R. Since the gradient of p_R always points toward the hotter edge of the layer, while the gradient of J_R reverses sign in the middle of the layer, there is necessarily a region where the sign of Eq. 13 is incorrect. In other words, there is a region where the radiation flows "uphill" toward regions of higher radiation energy density! In systems having optically thin hot (or cool) layers, no standard diffusion model will correctly solve for the detailed structure of the layer. Perhaps the simplest model that would do so would be one that would allow f_E to have spatial structure and would account for its derivatives. This conundrum is discussed in more detail in McClarren and Drake [67]. Nonetheless, typical diffusion models will correctly solve for most of the structure in these systems, because it is the overall flow of energy that determines this structure and because the magnitude of the fluxes are fundamentally set by energy conservation according to the arguments of the previous section.

5. Wall shocks and their effects

We now turn our attention to an aspect of these systems that involves their large-scale lateral structure produced by radiative effects. Some fraction of the upstream photon flux, of order several $\times 10^{28}$ photons/cm^2/s based on the parameters of Section 2, strikes the wall of the tube. Simple calculations show that this energy flux is not sufficient to drive a supersonic ionization front into the wall, or to heat the material that would be produced by such an ionization front. The consequence is that an "expansion heat front" develops, just as in an x-ray-driven inertial fusion capsule [63], in which the radiation is absorbed over a very small distance, creating a region of high pressure that drives a shock wave into the wall while producing a nearly isothermal rarefaction of material expanding from the wall into the gas.

This ablation of material from the plastic wall drives a *wall shock* into the Xe gas. This wall shock can be seen clearly in the data obtained using the most current techniques, such as that of Fig. 3. The shocked Xe near the wall then interacts with the primary shock moving down the tube. This is the origin of the "kink" seen in the primary shock. The properties of the shocks near this kink have implications for the local sound speed of the flow, as is discussed in the papers on wall shocks by Doss et al. [26] and Doss et al. [30]. In addition, the Xe gas that is first shocked by the expanding wall and then shocked in the region near the kink moves much more slowly (in the lab frame) than the post-shock flow behind the primary shock. The entrained flow behind the primary shock that is seen in the radiographs is attributed to this effect.

The entrained flow state's speed, direction, and compression can be predicted Doss et al. [30] by introducing the radiative shock relations discussed in Section 3 into the classical shock interaction theory Ben-Dor [68] to describe the radiative shocks in the system.

Fig. 6 shows graphically the procedure by which the entrained flow state is obtained. The plot is in the space of shock pressure-deflection polars, in which one may qualitatively compare the shape of the non-radiative (usual) wall shock and the (unusual, concave) radiative shocks. The shock polars describe possible states of flow passing through (1) the primary radiative shock of the system and (2) the wall shock and, subsequently, the deflected radiative shock between the kink and the wall. The pressure and flow deflections must be equivalent in these two cases, though the overall speed and other state variables may be different and can also be found through this method. Accordingly, in Fig. 6, the entrained flow state is the leftmost intersection of two of the shock polars. The predictions of this angle using this method match well with the data.

6. Simulation of driven radiative shocks

Our Center for Radiative Shock Hydrodynamics has been funded to model these experimental radiative shocks and to assess the predictive capability of the model. To do this, we have modified the Eulerian, adaptive BATSRUS numerical simulation code [69–71], which solves a nonlinear system of conservation laws and has good parallel scaling. The equations can be written as

$$\frac{\partial \mathbf{W}}{\partial t} + (\nabla \cdot \mathbf{G})^T = \mathbf{S}, \tag{16}$$

where **W** and **S** are state and source vectors, while **G** a flux dyad. For a given problem, all quantities are normalized with the help of physical quantities appropriate to the problem. The physical quantities include time t, position vector **r**, mass density, bulk flow velocity, total pressure, and total fluid internal energy density ϵ. For the work on radiative shocks, we take

$$\mathbf{W} = \begin{pmatrix} \rho \\ \rho\mathbf{u} \\ \epsilon + \frac{1}{2}\rho u^2 \\ \epsilon_e \end{pmatrix}, \tag{17}$$

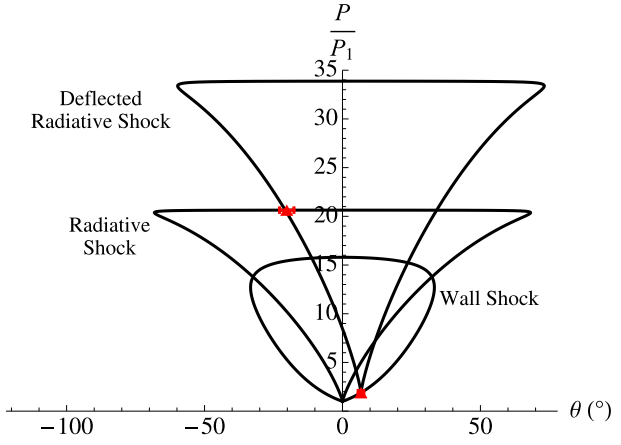

Fig. 6. Shock polars showing the locus of possible flow states achievable by passing through shocks in the space of pressure P (relative to upstream pressure) and flow direction θ (relative to axial flow). The polars shown are conditioned on the measurement (right red marker) of flow immediately downstream of the wall shock and are used to predict the state of the entrained flow immediately downstream of the kink leftmost intersection of "radiative shock" and "deflected radiative shock" polars, with the measurement (left red marker and error bars) of this angle. The data shown on this plot comes from Omega Shot 52665, calculated with $\gamma = 1.55$ and a primary shock speed of 110 km/sec. (For interpretation of the references to colour in this figure legend, the reader is referred to the web version of this article.)

$$\mathbf{G} = \begin{pmatrix} \rho\mathbf{u} \\ \rho\mathbf{u}\mathbf{u} + p\mathbf{I} \\ \mathbf{u}\left(\epsilon + \frac{1}{2}\rho u^2 + p\right) \\ \mathbf{u}\epsilon_e \end{pmatrix}, \quad \text{and} \tag{18}$$

$$\mathbf{S} = \begin{pmatrix} 0 \\ -\mathbf{S}_{rm} \\ \nabla.(C_e \nabla T_e) - S_{re} \\ S_e \end{pmatrix}. \tag{19}$$

Here ϵ_e is the internal energy density of the electron fluid. This internal energy affects the other hydrodynamic variables only indirectly through heat or radiation transport. The source vector **S** involves the radiation-electron momentum exchange term $\mathbf{S}_{rm}$, the radiation-electron energy exchange term $\mathbf{S}_{re}$, and electron heat conduction. We designate the code run with these specific equations as CRASH.

In CRASH we treat the radiation implicitly and in steady state, reflecting the reality that the radiation reaches steady state on a timescale much faster than that of the hydrodynamic evolution. Fundamentally, we integrate the radiation transfer equation given above over some number of frequency photon groups (typically 30), and solve a flux-limited radiation diffusion equation for each photon group. Then we integrate over the groups to obtain the net source terms needed by the state equations just given. Specifically, one finds S_{re} by integrating the radiation transfer equation over all solid angle and one finds $\mathbf{S}_{rm}$ by taking the first moment of this equation with direction of propagation. In **S** the coefficient of electron heat conduction is C_e. We ignore gravity, as is appropriate for the present application. Note that as usual in radiation hydrodynamics the electrons are assumed to be sufficiently coupled to the ions that the two species move together on average, although their temperatures may differ as a result of the differences in heating and cooling mechanisms for the two species. The electrons are heated or cooled by compression, heat conduction, radiation, and collisional energy exchange with ions. The electron heat source involves the electron pressure p_e and ion temperature T_i, and is given by

$$S_e = -p_e \nabla \cdot \mathbf{u} + \nabla \cdot (C_e \nabla T_e) - (S_{re} - \mathbf{S}_{rm} \cdot \mathbf{u}) + \frac{\rho k_B (T_i - T_e)}{A m_p \tau_{ei}}, \tag{20}$$

where m_p is the nucleon mass, A the atomic weight, k_B is the Boltzmann constant, and τ_{ei} is the electron–ion energy exchange timescale.

These equations require equation-of-state (EOS) relationships between ϵ and p; these also involve T_i and T_e and depend upon the average charge state Z of the ions. To date we have assumed equilibrium Equation-of-State (EOS) and ionization relations, derived from standard relations of statistical physics and from atomic data and accounting for the behavior of electrons as Fermions [72]. We then can write $\epsilon = \epsilon(p, \rho)$, $T_e = T_e(p, p)$, and $Z = Z(p, p)$. The coefficients C_e and τ_{ei} in the source terms, and the pressure, internal energy, and temperature of the ions are then functions of known parameters. The approach to material identity involves tracking a level-set function for each material. Each cell is identified with only a single material (there are no mixed cells), relying upon adaptive mesh resolution (AMR) to obtain adequate accuracy in this aspect. We likewise model the opacities self-consistently, based on the same statistical models and atomic data. As is discussed in Sokolov [72], this approach is an optimum one if one intends to quantify the uncertainties in the simulations, in spite of the fact that more ad hoc methods may provide the potential to tune the results to better approximate some specific experimental data.

We are at present implementing a "laser package" to account for laser energy deposition in a self-consistent way within a single simulation. In our work to date, however, we have used a two-dimensional, Lagrangian, radiation hydrodynamic code named Hyades [73] to evaluate the laser energy deposition and the behavior of the experimental system until the end of the laser pulse at 1.1 ns. At that time, we have mapped the Hyades output onto the Eulerian grid of CRASH and have run the evolution of the system out to the observation times of various experiments (up to 26 ns). The CRASH code is run in 2D with a reflecting boundary on the tube axis and outflow boundary conditions at other boundaries.

Fig. 7 shows a representative output of our current simulations. This simulation was run in 2D with an effective resolution of 4800 × 480 using two levels of mesh refinement, 30 radiation groups from 0.1 eV to 20 keV, and all the physics discussed above save for the laser package. The coloring of the upper left plot shows the material identity while the black lines show the locations where the mesh is dynamically refined, which are near material interfaces and the shock. The materials present on axis are Be (blue) and Xe (black). The wall includes gold (yellow), acrylic (red), and polyimide (green). One can see in the density plot (upper right) that the polyimide portion of the wall is thin; in the simulation the region outside this wall is modeled as polyimide at low density. In the density plot one can see the dense Xe in the primary shock and the wall shock ahead of the primary shock. One can also see the entrained Xe extending near the radial wall. In the density and other variables, one can see shocked Xe material clustering near the axis and protruding beyond the average position of the primary shock; we comment on this further below.

In the *X* velocity plot, one can see that at this time the highest velocity fluid is in the material near the shock and that the very highest velocity is in the protrusion near the axis. The *Y* velocity shows that material having the highest outward velocity is flowing outward along the shock away from the axis while at smaller radii there is some material flowing toward the axis. All the radial velocities are small compared to the fastest axial velocity, as one expects. Both the electron and ion temperature show the localized temperature spike in the cooling layer just behind the shock front, discussed in Section 2. Note that the scales are different. They allow one to see that the FWHM of the ion temperature spike is smaller than that of the electron temperature spike, as one expects. The quantity shown as radiation temperature is based on the total radiation energy density obtained by integrating over the energy groups. Because the cooling layer is optically thin there is no spike in the radiation temperature. This temperature decreases upstream of the shock because of the loss of radiative energy into the walls, causing the ablation that creates the wall shock.

In the pressure plot at the lower right, one can likewise see the layer of high pressure at the primary shock and the much lower pressure associated with the wall shock. When one examines the evolution of the system in time, one finds that during the first few ns, the expansion of the wall material drives a radially inward pressure pulse. This pressure pushes Be material to the axis, creating a pressure spike there that is connected with the emergence of material through the primary shock front near the axis. In the experimental data at this time (13 ns) there is no sign of a concentration of material near the axis or of any material protruding through the primary shock. This protrusion has been an enduring feature to date of simulations using CRASH initialized by Hyades, but has never yet been observed in the physical data. Extensive tests showed that numerical causes did not produce this effect and that it does not change significantly in three dimensional simulations. By modifying material properties such as the plastic opacity one can eliminate it, but this typically also eliminates the

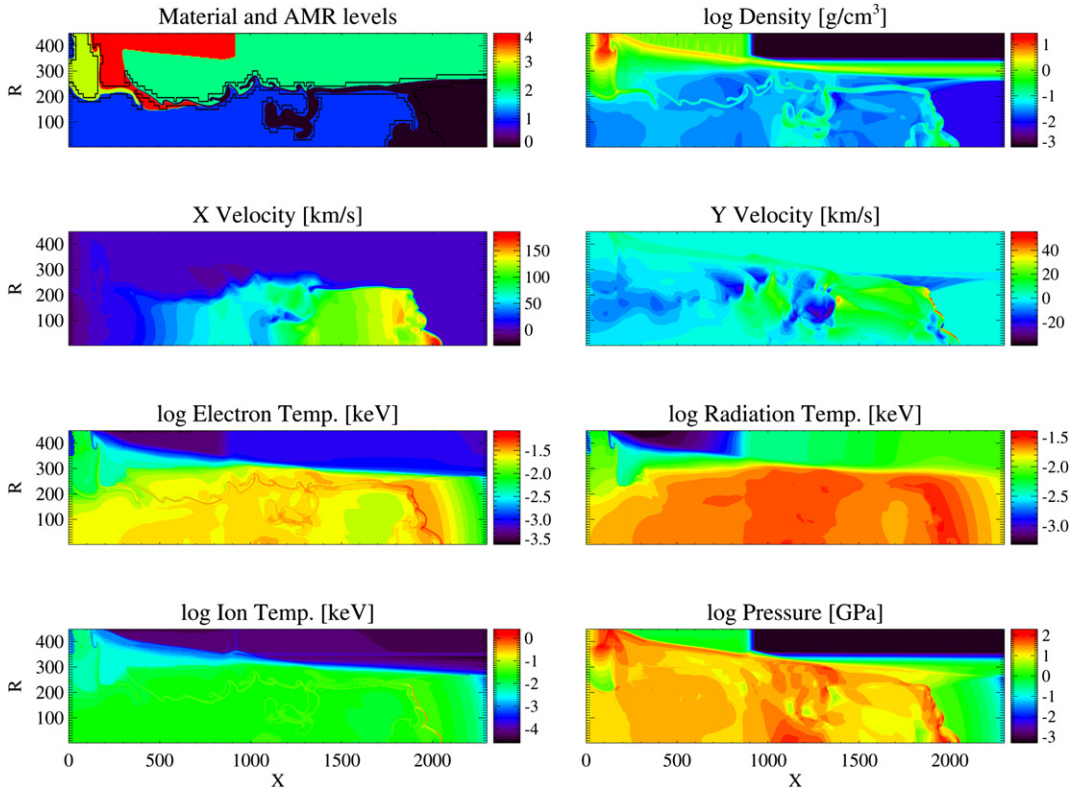

Fig. 7. Output at 13 ns of CRASH for the radiative shock experiment described in Section 2. Each plot shows a color map of the quantity designated above the plot, with the color bar providing the scale. All plots are functions of axial distance (*X*) and radial distance (*R*) as indicated, with distances given in microns.

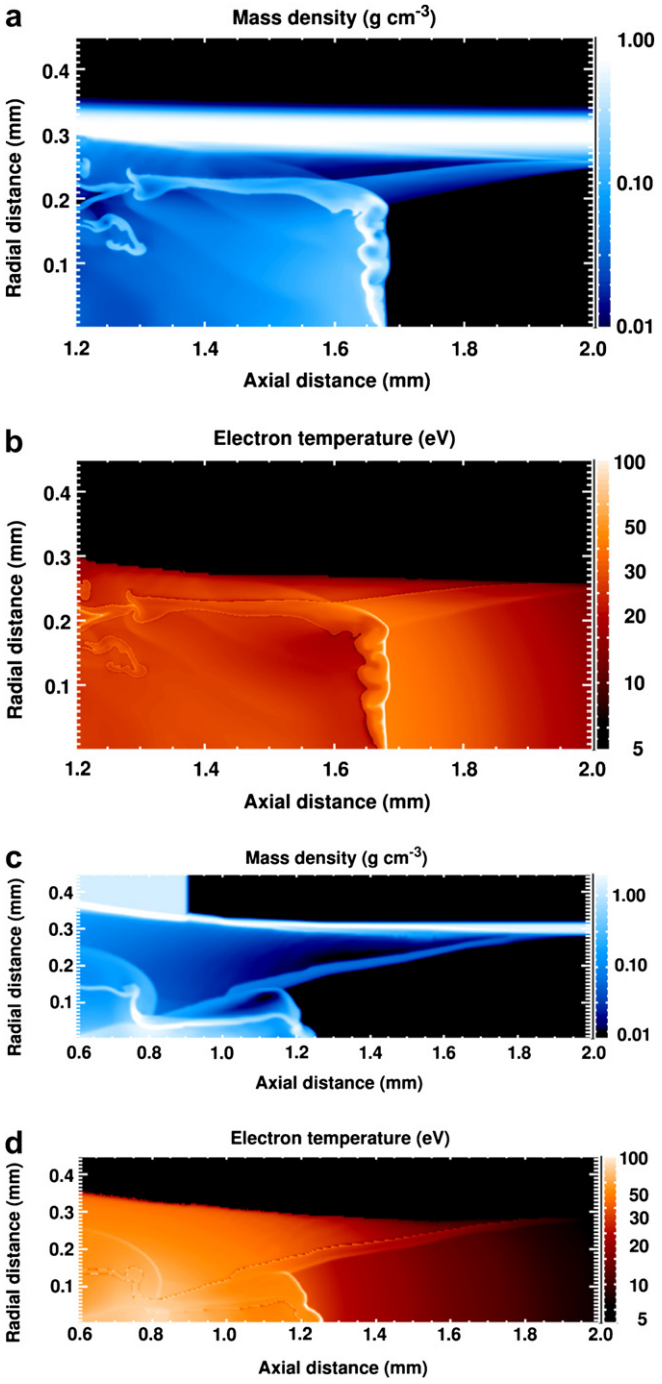

Fig. 8. CRASH simulations of potential x-ray-driven experiments at Omega (170 eV) and NIF (300 eV). (a) and (b) show density and electron temperature for a 170 eV x-ray drive on a 30 μm Be disk, at 13 ns. (c) and (d) show density and electron temperature for a 300 eV x-ray drive on a 55 μm Be disk, at 5 ns. Both simulations had 1200 × 120 resolution. All plots are functions of axial distance (X) and radial distance (R) as indicated, with distances given in mm.

wall shock. It remains unclear at the present writing whether this difference between code and data is due to the conditions established by Hyades or to insufficient fidelity in CRASH. Both codes use multigroup diffusion radiation transport, which will tend to deposit too much energy in the wall. Comparison with results using the CRASH laser package will better illuminate the origins of this difference. In addition, note that in the radiograph of Fig. 3 at 26 ns, one does see a concentration of shocked Xe near the axis. This suggests that an impulse directed toward the axis may be present in the experiment, even if much weaker than predicted by the simulations.

An alternative use of CRASH, that does not require input from any other code, is to model systems driven by thermal x-rays. One can find conditions that produce a primary shock and a wall shock without producing material that protrudes through the primary shock through the axis. One can even do this in a way that places the primary shock at the location where it is observed in the experiments, although this proves to delicately depend on the details. The first two panels in Fig. 8 show the density and electron temperature for this case. One can see the thin, hot, cooling layer in the electron temperature, the primary shock in the density, and the wall shocks in both panels. The characteristic shock velocity for this case is ∼150 km/s. The overall morphology seen is very similar to that shown in the laser-driven experiments of Fig. 3. One can also model systems with much larger shock velocities, as might be obtained on NIF. This case is shown in the bottom two panels of Fig. 8. The characteristic shock velocity for this case is ∼300 km/s. Here the wall shocks have converged on the axis, leading to a jet of Be and Xe that protrudes ahead of them.

The CRASH code has also proven useful in modeling potential new experiments designed to produce radiative reverse shocks, by causing a sufficiently fast flowing plasma to impact a solid surface. Issues include what diameter to make the shock tube and what radial structures will work best near the location of impact. We used CRASH to model this system, arriving at a design that worked well.

7. Conclusions

In the present paper we have discussed aspects of radiative shocks in shock tubes. Simple estimates of this dynamics reveal many of the properties found by more complex theories and simulations, including the creation of an optically thin cooling layer, of a dense shell of shocked material, and of secondary shocks from the tube wall ahead of the primary shock. In these systems, the kinetic energy entering the shock front provides the energy source for the behavior of the shock. However, blackbody radiation at the immediate postshock temperature would severely violate energy balance, and in response to this the system forms a cooling layer, of very small optical depth, through which the shocked matter cools to a viable final state by radiating a significant fraction of the incoming energy. A simple analysis of these dynamics and the energy balance establishes factor-of-two estimates of the final temperature and maximum compression.

At a next level of detail, theoretical models of the one-dimensional behavior reveal more clearly how aspects of the system are connected. Examination of the fluid equations shows that the fluid can access only unique states in which all of density, velocity, temperature, pressure, and radiation flux are determined. A consequence is that radiation transport cannot independently control any of these variables. For example, different models of radiation transport cannot change the density and temperature values that correspond to some specific net radiation flux. A closer examination of the radiation transport finds a remarkable property of these shocks, which is that an Eddington diffusion model with fixed Eddington factor cannot correctly model the radiation transport, because the relation between the pressure gradient and the gradient of mean radiation intensity changes sign within the cooling layer while the radiation flux does not change sign. Fortunately for simulations, the errors introduced in the present context because of this are small.

The radiation from the primary shock ablates the shock-tube wall ahead of it, causing expansion of the wall material that drives

a wall shock into the Xe gas in the tube. This wall shock interacts in turn with the primary shock, creating a deflected shock and a slip-stream interface that divides shocked Xe having different properties. The angles among these shocks can serve as a diagnostic of some local plasma parameters. In addition, the Xe shocked by the wall shock ends up moving more slowly than the Xe that first strikes the primary shock, creating an entrained shell of Xe behind the primary shock.

We have simulated our base experimental system using an implementation of our code, designated CRASH, that solves conservation equations in which the hydrodynamics is treated explicitly while the radiation and electron heat conduction are treated implicitly. These simulations reproduce the qualitative details of the system anticipated from the fundamental analysis and provide an evaluation for the structure of the cooling layer, the structure of the radiatively heated precursor ahead of the primary shock, and the detailed behavior of the walls that cannot be obtained from simple estimates. The simulations produce effects near the axis of the shock tube that are not observed in the experiments; their origin remains under exploration.

In future work, we intend to extend this type of experimental system to work with structures that are inherently three dimensional, such as elliptical shock tubes. This will create a more complex interplay of radiation and hydrodynamics and will provide demanding tests of three dimensional radiation hydrodynamic simulations. We also intend to continue the work with radiative reverse shocks mentioned briefly above. Beyond that, it would be of particular interest to develop an experimental system in which the inherent errors in typical Eddington diffusion models of optically thin hot or cool layers had substantial consequences.

Acknowledgments

This work was funded by the Predictive Sciences Academic Alliances Program in DOE/NNSA-ASC via grant DEFC52-08NA28616, by the DOE/NNSA-DS and DOE/SC-OFES Joint Program in High-Energy-Density Laboratory Plasmas, grant number DE-FG52-09NA29548, by the National Laser User Facility Program, grant number DE-FG52-09NA29034, by previous DOE grants and contracts, and by the University of Michigan.

References

[1] D.D. Ryutov, R.P. Drake, J. Kane, E. Liang, B.A. Remington, M. Wood-Vasey, Similarity criteria for the laboratory simulation of supernova hydrodynamics, Astrophys. J. 518 (1999) 821.
[2] L. Ensman, A. Burrows, Shock breakout in sn 1987a, Astrophys. J. 393 (1992) 742–755.
[3] C. Fransson, P. Lundqvist, R.A. Chevalier, Circumstellar interaction in sn 1993j, Astrophys. J. 461 (1996) 993–1008.
[4] T.K. Nymark, C. Fransson, C. Kozma, X-ray emission from radiative shocks in type ii supernovae, Astron. Astrophyhs 449 (2006) 171–192.
[5] K.J. Borkowski, J.M. Blondin, R. McCray, X-rays from the impact of sn1987a with its circumstellar ring, Astrophys. J. 477 (1997) 281–293.
[6] J.M. Blondin, E.B. Wright, K.J. Borkowski, S.P. Reynolds, Transition to the radiative phase in supernova remnants, Astrophys. J. 500 (1998) 342–354.
[7] B. Reipurth, J. Bally, Herbig-haro flows: probes of early stellar evolution, Ann. Rev. Astron, Astrophys 39 (2001) 403–455.
[8] J.C. Bozier, G. Thiell, J.P. Le-Breton, S. Azra, M. Decroisette, D. Schirmann, Experimental observation of the radiative wave generated in xenon by a laser-driven supercritical shock, Phys. Rev. Lett. 57 (1986) 1304–1307.
[9] P.A. Keiter, R.P. Drake, T.S. Perry, H.F. Robey, B.A. Remington, C.A. Iglesias, R.J. Wallace, J. Knauer, Observation of a hydrodynamically-driven, radiative-precursor shock, Phys. Rev. Lett. 89 (2002) 1–4 165003/.
[10] M. Koenig, A. Benuzzi-Mounaix, N. Grandjouan, V. Malka, S. Bouquet, X. Fleury, B. Marchet, C. Stehle, S. Leygnac, C. Michaut, J.P. Chieze, D. Batani, E. Henry, T. Hall, Radiative shock experiment using high power laser, in: M.D. Furnish, Y. Horie, N.N. Thadhani (Eds.), Shock Compression of Condensed Matter 2001, vol. 620, pt. 2 of AIP Conference Proceedings, American Institute of Physics, New York, Atlanta, Georgia, USA, 2002, pp. 1367–1370.
[11] X. Fleury, S. Bouquet, C. Stehl, M. Koenig, D. Batani, A. Benuzzi-Mounaix, J.P. Chize, N. Grandjouan, J. Grenier, T. Hall, E. Henry, J.P. Lafon, S. Leygnac, V. Malka, B. Marchet, H. Merdji, C. Michaut, F. Thais, A laser experiment for studying radiative shocks in astrophysics, Laser Part, Beams 20 (2002) 263–268.
[12] A.B. Reighard, R.P. Drake, K.K. Danneberg, D.J. Kremer, T.S. Perry, B.A. Remington, R.J. Wallace, D.D. Ryutov, J. Greenough, J. Knauer, T. Boehly, S. Bouquet, A. Calder, R. Rosner, B. Fryxell, D. Arnett, M. Koenig, N. Grandjouan, Collapsing radiative shocks in xenon gas on the omega laser. in: B.A. Hammel, D.D. Meyerhofer, J. Meyer-ter Vehn, H. Azechi (Eds.), Inertial Fusion and Science Applications. American Nuclear Society, New York, Monterey, CA, 2003, pp. 950–953.
[13] L. Boireau, C. Clique, S. Bouquet, Radiative shocks in low-pressure gases. in: B.A. Hammel, D.D. Meyerhofer, J. Meyer-ter Vehn, H. Azechi (Eds.), Inertial Fusion Science and Applications. American Nuclear Society, New York, Monterey, CA, 2003, pp. 966–969.
[14] T.W.L. Sanford, R.C. Mock, S.A. Slutz, D.L. Peterson, Length scaling of dynamic-hohlraum axial radiation, Phys. Plasmas 10 (2003) 4790–4799.
[15] S. Bouquet, C. Stehl, M. Koenig, J.P. Chize, A. Benuzzi-Mounaix, D. Batani, S. Leygnac, X. Fleury, H. Merdji, C. Michaut, F. Thais, N. Grandjouan, T. Hall, E. Henry, V. Malka, J.P.J. Lafon, Observations of laser driven supercritical radiative shock precursors, Phys. Rev. Lett. 92 (2004) 225001–225004.
[16] R.P. Drake, Radiative shocks in astrophysics and the laboratory, Astrophys. Space Sci. 298 (2005) 49–59.
[17] M. Koenig, T. Vinci, A. Benuzzi-Mounaix, S. Lepape, N. Ozaki, S. Bouquet, L. Boireau, S. Leygnac, C. Michaut, C. Stehle, J.P. Chieze, D. Batani, T. Hall, K. Tanaka, M. Yoshida, Radiative shock experiments at luli, Astrophys. Space Sci. 298 (2005) 69–74.
[18] T. Vinci, M. Koenig, A. Benuzzi-Mounaix, L. Boireau, S. Bouquet, S. Leygnac, C. Michaut, C. Stehle, O. Peyrusse, D. Batani, Density and temperature measurements on laser generated radiative shocks, Astrophys. Space Sci. 298 (2005) 333–336.
[19] A.B. Reighard, R.P. Drake, K.K. Dannenberg, D.J. Kremer, E.C. Harding, D.R. Leibrandt, S.G. Glendinning, T.S. Perry, B.A. Remington, J. Greenough, J. Knauer, T. Boehly, S. Bouquet, L. Boireau, M. Koenig, T. Vinci, Collapsing radiative shocks in xenon on the omega laser, Phys. Plasma 13 (2006) 082901.
[20] T. Vinci, M. Koenig, A. Benuzzi-Mounaix, C. Michaut, L. Boireau, S. Leygnac, S. Bouquet, O. Peyrusse, D. Batani, Temperature and electron density measurements on laser driven radiative shocks, Phys. Plasma 13 (2006) 010702.
[21] M. Koenig, T. Vinci, A. Benuzzi-Mounaix, N. Ozaki, A. Ravasio, M.R.I. Glohaec, L. Boireau, C. Michaut, S. Bouquet, S. Atzeni, A. Schiavi, O. Peyrusse, D. Batani, Radiative shocks: An opportunity to study laboratory astrophysics, Phys. Plasmas 13 (2006) 056504.
[22] A.B. Reighard, R.P. Drake, J.E. Mucino, J.P. Knauer, M. Busquet, Planar radiative shock experiments and their comparison to simulations, Phys. Plasma 14 (2007) 056504–056508.
[23] A.B. Reighard, R.P. Drake, The formation of a cooling layer in a partially optically thick shock, Astrophys, Space Sci. 307 (2007) 121–125.
[24] C. Michaut, T. Vinci, L. Boireau, M. Koenig, S. Bouquet, A. Benuzzi-Mounaix, N. Osaki, G. Herpe, E. Falize, B. Loupias, S. Atzeni, Theoretical and experimental studies of radiative shocks, Astrophys. Space Sci. 307 (2007) 159–164.
[25] M. Busquet, E. Audit, M. Gonzalez, C. Stehle, F. Thais, O. Acef, D. Bauduin, P. Barroso, B. Rus, M. Kozlova, J. Polan, T. Mocek, Effect of lateral radiative losses on radiative shock propagation, High Energy Density Phys. 3 (2007) 8–11.
[26] F.W. Doss, H.F. Robey, R.P. Drake, C.C. Kuranz, Wall shocks in high-energy-density shock tube experiments, Phys. Plasma 16 (2009) 112705.
[27] M. Gonzalez, E. Audit, C. Stehle, 2d numerical study of the radiation influence on shock structure relevant to laboratory astrophysics, A&A 497 (2009) 27–34.
[28] F.W. Doss, R.P. Drake, C.C. Kuranz, Repeatability in radiative shock tube experiments, High Energy Density Phys. 6 (2010) 157–161.
[29] F.W. Doss, C.C. Kuranz, R.P. Drake, Statistical inference in the presence of an inclination effect in laboratory radiative shock experiments, Astrophys, Space Sci (2011) in press.
[30] F.W. Doss, R.P. Drake, E.S. Myra, Oblique radiative shocks, including their interactions with non-radiative polytropic shocks, Physics of Plasmas, in press.
[31] J. Grun, J. Stamper, C. Manka, J. Resnick, R. Burris, J. Crawford, B.H. Ripin, Instability of taylor-sedov blast waves propagating through a uniform gas, Phys. Rev. Lett. 66 (1991) 2738–2741.
[32] J.M. Laming, J. Grun, Dynamical overstability of radiative blast waves: The atomic physics of shock stability,, Phys. Rev. Lett. 89 (2002) 125002–125005.
[33] J.F. Hansen, M.J. Edwards, D.H. Froula, A.D. Edens, G. Gregori, T. Ditmire, Secondary shock formation in xenon-nitrogen mixtures, Physic. Plasma 13 (2006).
[34] J.F. Hansen, M.J. Edwards, D.H. Froula, A.D. Edens, G. Gregori, T. Ditmire, Laboratory observation of secondary shock formation ahead of a strongly radiative blast wave, Astrophys. Space Sci. 307 (2007) 219–225.
[35] M.J. Edwards, A.J. MacKinnon, J. Zweiback, K. Shigemori, D.D. Ryutov, A.M. Rubenchik, K.A. Keitlty, E. Liang, B.A. Remington, T. Ditmire, Investigation of ultrafast laser-driven radiative blast waves, Phys. Rev. Lett. 87 (2001) 085004–1–085004–4.
[36] A.S. Moore, E.T. Gumbrell, J. Lazarus, M. Hohenberger, J.S. Robinson, R.A. Smith, T.J.A. Plant, D.R. Symes, M. Dunne, Full-trajectory diagnosis of

laser-driven radiative blast waves in search of thermal plasma instabilities, Phys. Rev. Lett. 100 (2008).
[37] M. Hohenberger, D.R. Symes, J. Lazarus, H.W. Doyle, R.E. Carley, A.S. Moore, E.T. Gumbrell, M.M. Notley, R.J. Clarke, M. Dunne, R.A. Smith, Observation of a velocity domain cooling instability in a radiative shock, Phys. Rev. Lett. 105 (2010).
[38] D.R. Symes, M. Hohenberger, J. Lazarus, J. Osterhoff, A.S. Moore, R.R. Faustlin, A.D. Edens, H.W. Doyle, R.E. Carley, A. Marocchino, J.P. Chittenden, A.C. Bernstein, E.T. Gumbrell, M. Dunne, R.A. Smith, T. Ditmire, Investigations of laser-driven radiative blast waves in clustered gases, High Energy Density Phys. 6 (2010) 274–279.
[39] I.B. Zel'dovich, Shock waves of large amplitude in air, Soviet Phys. JETP 5 (1957) 919.
[40] Y.P. Raizer, On the structure of the front of strong shock waves in gases, Soviet Phys. JETP 5 (1957) 1242–1248.
[41] C. Michaut, E. Falize, C. Cavet, S. Bouquet, M. Koenig, T. Vinci, A. Reighard, R.P. Drake, Classification of and recent research involving radiative shocks, Astrophys. Space Sci. 322 (2009) 77–84.
[42] Y.B. Zeldovich, Y.P. Razier, Physics of Shock Waves and High-temperature Hydrodynamic Phenomena. Academic Press, New York, dover, 2002, vol. 1edition, 1966.
[43] D. Mihalas, B. Weibel-Mihalas, Foundations of Radiation Hydrodynamics. Oxford University Press, Oxford, dover, 1999, vol. 1edition, 1984.
[44] A.V. Farnsworth, J.H. Clarke, Radiatively and collisionally structured shock waves exhibiting large emission-convection ratio, Phys. Fluids 14 (1971) 1352–1360.
[45] R.I. Klein, R.F. Stein, W. Kalkofen, Radiative shock dynamics. i. the Lyman continuum, Astrophys. J. 205 (1976) 499–519.
[46] R.I. Klein, R.F. Stein, W. Kalkofen, Radiative shock dynamics. II. Hydrogen continua, Astrophys. J. 220 (1978) 1024–1040.
[47] E. Bertschinger, On the structure and stability of radiative shock waves, Astrophys. J. 304 (1986) 154–177.
[48] S. Bouquet, R. Teyssier, J.P. Chieze, Analytical study and structure of a stationary radiative shock, Astrophys, J. Suppl. 127 (2000) 245–252.
[49] R.P. Drake, Theory of radiative shocks in optically thick media, Phys. Plasma 14 (2007a) 043301–043310.
[50] R.P. Drake, Energy balance and structural regimes of radiative shocks in optically thick media, IEEE Trans. Plasma Sci. 35 (2007) 171–180.
[51] R.B. Lowrie, R.M. Rauenzahn, Radiative shock solutions in the equilibrium diffusion limit, Shock Waves 16 (2007) 445–453.
[52] R.B. Lowrie, J.D. Edwards, Radiative shock solutions with grey nonequilibrium diffusion, Shock Waves 18 (2008) 129–143.
[53] R.A. Chevalier, J.C. Theys, Optically thin radiating shock waves and the formation of density inhomogeneities, Astrophys. J. 195 (1975) 53–60.
[54] F.H. Shu, The Physics of Astrophysics: Gas Dynamics. University Science Books, Mill Valley, CA, 1992, vol. II.
[55] R.A. Chevalier, J.N. Imamura, Linear-analysis of an oscillatory instability of radiative shock-waves, Astrophys. J. 261 (1982) 543–549.
[56] D.E. Innes, J.R. Giddings, S.A.E.G. Falle, Dynamical models of radiative shocks, II. Unsteady shocks, MNRAS 226 (1987) 67–93.
[57] R.G. McClarren, R.P. Drake, M.L. Adams, J.E. Morel, J.P. Holloway, Theory of radiative shocks in the mixed, optically thick-thin case, Phys. Plasma 17 (2010) 093301.
[58] J.P. Holloway, D. Bingham, C.C. Chou, F.W. Doss, R.P. Drake, B. Fryxell, M.J. Grosskopf, B.v.d. Holst, B. Mallick, R.G. McClarren, A. Mukherjee, V. Nair, K.G. Powell, D. Ryu, I. Sokolov, G. Toth, Z. Zhang, Predictive modeling of a radiative shock system, Reliab. Eng. Syst. Saf., in press.
[59] R.G. McClarren, D. Ryu, R.P. Drake, M.J. Grosskopf, D. Bingham, C.C. Chou, B. Fryxell, B.v.d. Holst, J.P. Holloway, C.C. Kuranz, B. Mallick, E. Rutter, B.R. Torralva, A physics informed emulator for laser-driven radiating shock simulations, Reliab. Eng. Syst. Saf., in press.
[60] M.J. Grosskopf, D.C. Marion, R.P. Drake, C.C. Kuranz, F.W. Doss, A.J. Visco, C.M. Huntington, C.A. Krauland, C.A. Di Stefano, E.C. Harding, Target fabrication at the University of Michigan, Fus. Sci. Technol 59 (2011) 250–256.
[61] C.C. Kuranz, B.E. Blue, R.P. Drake, H.F. Robey, J.F. Hansen, J.P. Knauer, M.J. Grosskopf, C. Krauland, D.C. Marion, Dual, orthogonal, backlit pinhole radiography in omega experiments, Rev. Sci. Inst 77 (2006) 1–4 10E327.
[62] T.R. Boehly, R.S. Craxton, T.H. Hinterman, J.H. Kelly, T.J. Kessler, S.A. Kumpman, S.A. Letzring, R.L. McCrory, S.F.B. Morse, W. Seka, S. Skupsky, J.M. Soures, C.P. Verdon, The upgrade to the omega laser system,, Rev. Sci. Intsr 66 (1995) 508–510.
[63] R.P. Drake, High Energy Density Physics: Fundamentals, Inertial Fusion and Experimental Astrophysics. Springer, Verlag, 2006.
[64] E.T. Vishniac, The dynamic and gravitational instabilities of spherical shocks, Astrophys. J. 274 (1983) 152–167.
[65] E. Ott, Nonlinear evolution of the Rayleigh-Taylor instability of a thin layer, Phys. Rev. Lett. 29 (1972) 1429–1432.
[66] F.W. Doss, Structure in Radiative Shock Experiemnts, Ph.D. thesis, University of Michigan, 2011.
[67] R.G. McClarrenR.P. Drake, Radiative transfer in the cooling layer of a radiating shock, J. Quant. Spectrosc. Radiat. Transf 111 (2010) 2095–2105.
[68] G. Ben-Dor, Shock Wave Reflection Phenomena, second ed., Springer, 2007
[69] K.G. Powell, P.L. Roe, T.J. Linde, T.I. Gombosi, D.L.D. Zeeuv, A solution-adaptive upwind scheme for ideal magnetohydrodynamics,, J. Comput. Phys. 154 (1999) 284–309.
[70] G. Toth, D. Kovacs, K.C. Hansen, T.I. Gombosi, Three-dimensional MHD simulations of the magnetosphere of Uranus, J. Geophys. Res.-Space Phys. 109 (2004) 0148–0227 A11210.
[71] B. van der Holst, G. Toth, I.V. Sokolov, K.G. Powell, J.P. Holloway, E.S. Myra, Q. Stout, M.L. Adams, J.E. Morel, R.P. Drake, A block-adaptive-mesh code for radiative shock hydrodynamics: Implementation and verification, Astrophys. J. Suppl. Ser., in press.
[72] I.V. Sokolov, R.P. Drake, A trivially correct model for equations of state and opacities, High Energy Density Phys., in preparation.
[73] J.T. Larsen, S.M. Lane, Hyades: a plasma hydrodynamics code for dense plasma studies, J. Quant. Spectrosc. Radiat. Transf 51 (1994) 179–186.